Invariant synaptic density across species

André Ferreira Castro,[1,2,3*] Albert Cardona,[1,2]

[1]Neurobiology Division, MRC Laboratory of Molecular Biology,
Francis Crick Avenue, Cambridge Biomedical Campus,
Cambridge, CB2 0QH, UK
[2]Department of Physiology, Development and Neuroscience,
University of Cambridge, Cambridge, CB2 3DY, UK
[3]Current Address: School of Life Sciences,
Technical University of Munich, Freising, 85354Germany

*To whom correspondence should be addressed; E-mail: acastro@mrc-lmb.cam.ac.uk

July 18, 2024

We measured neuronal cell structure and connectivity from fly and zebrafish to mouse and human and discovered an invariant feature: an average of one synapse for every micrometer of dendritic cable. We provide evidence of how this pattern emerges from precise spatial positioning, electrical activity, and resource conservation in neurons. Our results imply that nervous systems converged onto synaptic density invariance to stabilise neuronal responses, suggesting a simplifying principle for neural circuit function, assembly and evolution.

Introduction

Body size varies by 21 orders of magnitude in the animal kingdom (*1*). In contrast to most animal organs, which scale through the proliferation of dividing cells of similar size, brains expand by modulating the size of non-dividing neuronal cells to innervate space during development (*2–4*). As a result, there is notable diversity in neuronal size and structure within individual brains and between different species (*5–7*). Considering that size inherently affects the rates of all biological processes and structures, from cellular metabolism to information processing (*8–10*), the ability of neurons to maintain essential computational functions despite variation in size remains a crucial and unresolved question in neuroscience (*11–13*).

Synaptic density convergence across species

As shown in **Figure 1A-B**, synaptic dendritic cable density (hereafter synaptic density) across different cell types in *Drosophila*, zebrafish, and mouse nervous systems converges to approximately $\frac{1syn}{\mu m}$ of dendritic cable (overall mean = $\frac{0.92syn}{\mu m} \pm 0.29$; *D.* larva mean = $\frac{0.96syn}{\mu m} \pm 0.34$; *D.* adult mean = $\frac{0.8syn}{\mu m} \pm 0.2$; zebrafish mean = $\frac{0.76syn}{\mu m} \pm 0.23$; mouse mean = $\frac{0.99syn}{\mu m} \pm 0.28$; **Table 1**; **Figure S1**; see Methods for the specific lower density in zebrafish) (*14–18*). Interestingly, this convergence persists despite variations in dendritic lengths, circuits, and ecological niches. In particular, in the most densely reconstructed datasets, specifically *Drosophila* larva and mouse, the correspondence with $\frac{1syn}{\mu m}$ is remarkably robust, with no statistical difference found between them (difference of the means $= \frac{0.031syn}{\mu m}$, permutation test $p = 0.13$). Adding human data from a recent study further substantiates this pattern (data from (*19*), mean estimate $=\frac{0.91syn}{\mu m}$; **Figure 1B**). This finding is unexpected considering that earlier volumetric density studies revealed significant variations in synapse density per volume across different circuits in various species (*20–22*). Moreover, previous research suggested that human neurons have higher synaptic densities to support their complex functions (*23, 24*)

Functional implications of invariant synaptic density in scaling nervous systems

Since synaptic distribution is integral to single-cell computation, invariance in synaptic density raises the question: What are its functional implications in scaling nervous systems (*25, 26*)? Recent theoretical studies have shown that neuronal firing rates remain stable in a wide range of dendritic morphologies in response to distributed synaptic inputs. This consistent pattern of activity is observed regardless of the branching pattern, size, or synaptic spatial distribution in dendritic trees (*27*). Such firing rate stability depends primarily on synaptic density. In particular, for a given synaptic density, if the average dendritic radius and membrane conductivity are consistent across neurons, the effect becomes more significant. The output spiking rate R can then be approximated by $R \approx IF_{syn} + c$, where IF_{syn} represents the input fraction of activated synapses (as a percentage of total postsynapses) and c is a constant (*27*). Such connectivity and morphology independent point-like neurons endow networks with the capacity to maintain functional robustness due to normalisation effects (*28–30*), paralleling methods employed in machine learning (*31, 32*).

Dendrite development and synaptic density

Given the observed invariance in synaptic density across species, we analysed the relationship between neuronal arbour development and the establishment of the appropriate number of synapses during circuit wiring. Prior work in *Drosophila* (*33–35*), *C. elegans* (*36*) and mouse (*37*) showed that synaptic density remains constant despite steep increases in the number of synapses throughout development. These findings pointed to intrinsic mechanisms that regulate synaptic density during development (*38*). To further investigate this, we analysed the synaptic density in the neuronal morphologies of wild-type and mutant mechano-sensory neurons in *D.* larvae reconstructed from EM data (*39*). These mutants carry genetic constructs that

either shift arbour locations (*Mechano-FraRobo*) or silence their activity (*Mechano-TNT*), and had been analysed for effects on synaptic connectivity (**Figure S2A**; see Methods). We found that while wild-type morphologies exhibit synaptic densities close to $\frac{1syn}{\mu m}$ (mean = $\frac{0.87}{\mu m} \pm 0.12$), both mutants have significantly lower densities (*Mechano-FraRobo* mean = $\frac{0.65}{syn/\mu m} \pm 0.09$, $p < 0.001$; *Mechano-TNT* mean = $\frac{0.59}{syn/\mu m} \pm 0.12$, $p < 0.001$; **Figure 1C**). Despite large and significant differences in synaptic density, mutant dendritic morphologies were not significantly different from wild-type ones, indicating that the effect is independent of overall arbour morphology (**Figure S2B-E**). These findings underscore the need for precise spatial positioning and neuronal activity during development to establish appropriate synaptic connectivity and density (*40, 41*).

Factors influencing synaptic density variability

Why does synaptic density vary around the mean of $\frac{1\text{syn}}{\mu\text{m}}$? Although noisy developmental processes and measurement and sampling errors (*42*) account for some of the observed variance, cell-type specific factors are known to impact neuron excitability. These factors include anatomical differences in dendritic radius, synapse strength, and variations in the composition of ion channels (*43–49*). Interestingly, recent work has shown that species with thicker dendrites exhibit higher membrane ionic conductances, leading to a conserved conductance per unit of brain volume that helps maintain stable neuron excitability across scales (*50*). Thus, we hypothesise that other factors such as radius and synaptic strength synergise with synaptic density in a compensatory manner to achieve homeostasis of neuronal activity (**Figure 2A**).

In fact, our analysis reveals two patterns that support this hypothesis. First, mouse data shows that synaptic density correlates with dendrite radius ($r = 0.67, p = 0$; **Figure 2B**), potentially maintaining neuronal excitability stable as input resistance changes due to variations in mean radii (*27*). This correlation could explain reports of slightly higher values of synaptic

density in mouse data than $\frac{1\text{syn}}{\mu\text{m}}$ (*19, 51*). However, this strategy becomes self-defeating between species. Given synaptic density invariance across species, coupled with the fact that the dendritic radius in larger brains is slightly thicker to mitigate conduction delays, what alternative factors could compensate for lower input resistance (*52*)? Specifically, the mean size of the synapse, measured by the area of postsynaptic densities (PSD) as a proxy of synaptic strength (*53*), shows a significant correlation with the average dendritic radius between species ($r = 0.88, p = 0.018$; **Figure 2C**; **Table 2, 3**). This correlation implies that variations between species in synaptic strength can offset differences in neuronal excitability resulting from variation in dendritic radii. In general, these observations suggest a biophysical mechanism that maintains the stability of neuronal activity, regardless of variations in scale and connectivity.

Another source of fluctuations in synaptic densities in mature cells is plasticity (*54*). Recognising the static nature of EM imaging, it is plausible to assume that, at the time of acquisition, the variability in synaptic density between neurons could reflect different stages or outcomes of neural plasticity (distinct from developmental synaptic pruning; (*55, 56*)). However, dendrites are known to use structural homeostasis to conserve synaptic numbers or overall input strength, while the relative strength of specific inputs is modified (*37, 40, 41, 57–61*). These studies suggest that the magnitude of plasticity-induced fluctuations is likely small, consistent with the relatively low variability we observed in synaptic densities.

Impact of synaptic size on density

A key question is why neurons exhibit a specific synaptic density of $\frac{1syn}{\mu m}$. We draw insights from the following findings. First, cable optimisation theory work revealed that, to minimise signal delays, synaptic packing (the volume occupied by synaptic structures) should not disturb the optimal "$\frac{3}{5}$" ratio that axon-dendrite volumes take up from total tissue from (*62*). Thus, we reasoned that optimal packing tightly regulates the "volume budget" that synapses can occupy

in a circuit. However, packing a large number of small synapses, vs. a smaller number of large synapses, impacts dendritic synaptic density in opposite ways (**Figure S3A**). Then can optimal packing force synaptic density to the observed $\frac{1syn}{\mu m}$? To test this in mouse data (*18*), the only dataset for which synaptic size information was available in all morphologies, we calculated the total volume occupied by synapses in the circuit. Then, we distributed the volume budget across "synapses" of sizes that varied incrementally while computing synaptic density. We found that volume conservation creates a wide distribution of possible synaptic density values (**Figure S3B**; lower bound = $\frac{0.25syn}{\mu m}$, upper bound = $\frac{19.56syn}{\mu m}$; see Methods). To better understand the relationship between the size of the synapses and the density, we calculated the correlation between the mean size of the synapses and the density of each neuron in the same data set. The results showed a low negative correlation (**Figure S3C**; $r = -0.29, p = 0$). Together, these results indicate that the invariance of the synaptic density is not imposed by packing constraints, and why the average between species is $\frac{1syn}{\mu m}$ remains unexplained.

Synaptic density invariance conforms with wiring optimisation principles

Geometric constraints between neurite cable and volume point to an answer. The scaling relationship between the length of the dendritic cable (L) and the volume occupied (V) in a circuit is generally expressed by the scaling law $L \approx \sqrt[3]{\frac{3}{4*\pi}} \cdot \sqrt[3]{V} \cdot n^{\frac{2}{3}}$, where ($n$) represents the number of synapses connected with minimal dendritic cable (*63, 64*) (**Figure 1A**; **Figure 3A**). We compared the measured dendrite length with the result of predicting dendrite length with this scaling law, and found that dendritic trees across species scale using minimum cable resources (**Figure 3B**, **S4**; Pearson correlation $r = 0.87$, $p = 0$; see **Table 4** for which datasets were used). With this scaling law, we now challenge the invariant synaptic density hypothesis with a sensitivity analysis whereby we incrementally vary synaptic density (**Figure 3A**). We quantified the agreement between observed dendritic lengths and theoretical expectations by using

the Euclidean distance as a metric (see Methods). This analysis revealed an inflection point at a density of $1 - 1.1 syn/\mu m$, where the discrepancy between theoretical predictions and observed data is minimised, which coincides with the average observed synaptic density (**Figure 3B**). The close alignment between theory and experimental data suggests that the observed synaptic density of $\frac{1syn}{\mu m}$ is not an artefact of EM imaging and suggests that universal wiring minimisation principles shape synaptic density and dendritic structure (*65*).

Discussion

Having established synaptic density invariance across neuronal types and species, we now consider the implications for neural coding. Theory proposes that, despite variations in the structure and size of neuronal arborisations, as long as synaptic density remains constant, neuronal spike rates remain stable (*27*). This stability also preserves the ability to modulate the timing of spikes (*27, 34*). Maintaining a stable firing rate is crucial for reliable computations that rely on spike timing, since it provides a consistent background against which temporal variations can be effectively encoded. (*66–68*). Therefore, synaptic density invariance may support cell-type specific spike-time modulation (*27, 60, 67, 69–71*). All together, we propose that the invariant average synaptic density of $\frac{1syn}{\mu m}$ represents an optimal set point for both brain architecture and computational reliability of neurons, while minimising resources as the nervous system scales in development and evolution (*12*).

From dendrites to point neurons

Our findings inform an ongoing debate in neuroscience. Dendritic complexity has been considered crucial for understanding brain function (*25, 26, 72, 73*), however, both simplified models of neural circuits and machine learning research have achieved remarkable success with networks of point neurons, (*32, 74, 75*) abstracting away cellular detail. Our data and analysis supports

the use of point neurons as useful abstractions of what nature – across species and scales – converged on to maintain a stable rate code.

Methods

Electron microscopy data and morphologies

Morphologies were obtained from five electron microscopy volumes encompassing the central or peripheral nervous systems of four distinct species, including one first instar *Drosophila melanogaster* larva (*14, 15, 76*), one adult *Drosophila melanogaster* (*77*), one larval Zebrafish (*Danio rerio*; (*16*)), and finally two adult mice (*Mus musculus*; (*17, 18*)). These datasets were selected because they were densely reconstructed and annotated or proofread by experts.

From the larval insect datasets, neurons were selected based on the reconstruction level of the corresponding cell types (**Table 1**). Although the larval complete connectome has been released, only a few brain regions have been fully reconstructed and have all anatomical synapse sites annotated (*78*). To maintain consistency across the brains of larval and adult flies, we pooled the same cell types from the Hemibrain dataset. However, the levels of postsynaptic reconstruction for some of these cell types were low, which highly correlated with synaptic density ($r = 0.61, p = 0$, **Figure S1D**). To circumvent this issue and avoid bias in our analysis, we discarded cell types with postsynaptic reconstruction levels below 80%. To increase the sample size, we searched for other regions of the brain with adequate levels of reconstruction. This search yielded another brain region that satisfied this constraint, the ellipsoid body. For the case of the ellipsoid neurons, we included all neurons marked as fully traced.

To test the hypothesis of dendritic synaptic density invariance, additional data was analysed spanning 4 volumes of electron microscopy (**Table 1**), including two *Drosophila melanogaster* larva mutants (*FraRobo* and tetanus toxin light chain *TNT*; (*39*)), and data from two cerebral cortices of humans (*19*). From (*19*), human neuron morphologies were not used directly because the data was not released; instead, only estimates of synaptic counts in dendritic trees and the total length of dendritic trees of the available cell types were considered to compute the general

dendritic synaptic density.

Measurement of dendritic radius

To measure dendritic radii, we used data from the aforementioned electron microscopy (EM) and additional light microscopy datasets pooled from the neuromorpho database (**Table 1**; (*79*); `neuromorpho.org`). For the EM datasets, raddi data were readily available from three EM volumes of two distinct species, adult *Drosophila melanogaster* (*77*), and two adult mice (*Mus musculus*; (*17, 18*)).

In the case of the *Drosophila* larva EM dataset, the radius information was missing. To address this, we used a custom tool in CATMAID (*80*) to manually trace the radius of 20 full dendrites of Kenyon cells (KC) from the mushroom body (MB). To enhance the representation of our dataset, we first computed the mean radius of the nodes for each Strahler order of manually traced dendrites (*81, 82*). Next, we determined the Strahler number for all other KC dendritic nodes in the mushroom body (MB). Using the mean radius value corresponding to each Strahler order, we assigned these values to each node of the non-traced KCs dendrites. We then calculated the mean radius value on the entire KCs dataset ($N = 150$). Thus, ensuring a consistent and representative measurement across the dataset.

From the light microscopy datasets, we included data from both humans (*83*) and rats (*84*) to match the available ultrastructural postsynaptic density (PSD). For the rat dataset, it was possible to match LM morphologies with areas of the brain where PSDs were quantified. However, for human data, it was not possible to match the LM morphologies to the specific brain regions where the PSDs were obtained. Therefore, we sampled all available morphologies from the NeuroMorpho database to avoid sampling biases. Similarly to EM datasets, only data annotated with complete 3D dendritic reconstruction status were used to compute the dendritic radius.

Measurement of postsynaptic density

Postsynaptic density (PSD) areas were obtained from various EM volumes that encompass the synapses of the central or peripheral nervous systems of four distinct species (Table 3), including first instar *Drosophila melanogaster* (larva and adult) (*85*), mouse (*53*), rat (*86*) and human (*87*). These data sets were selected because they provide ultrastructural resolution data on PSD areas, which is a strong anatomical proxy of synaptic strength (*53*).

For the adult *Drosophila melanogaster* dataset, we collected PSD areas following the procedure described by (*85*) for synapses of interest from the FAFB dataset (*88*). Shortly, using a CATMAID's Python interface, we extracted the locations of synaptic contacts between neurons of interest. With BigCAT (`https://github.com/saalfeldlab/bigcat`), a BigDataViewer-based volumetric annotation tool, we annotated the postsynaptic membrane across EM slices. The synaptic surface area is represented by all visible membrane sections, measured in nm^2. The total area of a synapse is approximated by summing these areas for a single contact across z sections.

Neuronal morphologies and skeletonization

Electronic microscopy neuronal skeletons for adult and larval *Drosophila melanogaster* were obtained from `virtualflybrain.com` using custom Python and R scripts. Mouse neuronal arbor morphologies were obtained by downloading them from `https://www.MICrONS-explorer.org` or requesting them directly from the authors of the original studies (*18*). In the case of larval zebrafish, skeletons were derived from the meshes of the corresponding neuron morphologies provided by the authors of the original study (*16*). These meshes were imported into the Navis environment `https://github.com/navis-org/navis`), where we extracted the spatial coordinates of each skeleton node along with soma identifiers for further analysis. For the case of light microscopy data, neuronal skeletons were obtained from the

neuromorpho database ((*79*); neuromorpho.org).

Next, all skeletons were imported into the TREES Toolbox (MATLAB; https://www.treestoolbox.org) for quality assurance, in a two-step process. Initially, we used specific inbuilt functions in TREES Toolbox to verify data integrity, followed by a visual inspection by two expert annotators. In some cells, the ambiguity in the location of the soma within the representations of the skeleton was resolved through manual consensus of two expert annotators, who used cell type-specific anatomical features and radius information to estimate the correct location of the soma. Neurons with persistent ambiguity after proofreading, mainly due to artefacts, were excluded from the analysis, generating a total number of skeletons $N = 2863$, for all species (**Table 4**).

In the larval zebrafish dataset, we noted that some skeletons presented cycles in their graph representation, a common error when segmentation-based proofreading is used for skeletonisation. This error typically arises due to the addition of false side branches in voluminous neuronal parts such as the soma, or due to image artefacts or masking issues. To address this, we first resampled the trees to sampling nodes of $1\mu m$ and then used a previously described minimum-spanning tree (MST)-based algorithm to reconnect the nodes to skeletons (*89*). This effectively maintained the original tree's topology and geometry while eliminating cycles from the graph structure.

Finally, all EM-derived data, namely skeletons, synapse, and soma location data, were imported into Navis (Python, https://github.com/navis-org/navis), Natverse (R, (*90*)), or TREES Toolbox for subsequent analysis, and were rescaled to 1x1x1 μm. Custom Python, R, and MATLAB scripts were employed for skeleton analysis and statistics, performed within the aforementioned environments, facilitating analysis. All analysis scripts and files related to neuronal morphology and synapse locations will be included in the Supplemental Data after publication.

Distinguishing axons and dendritic compartments in neuronal trees

To accurately test the predictions from the dendritic synaptic density, synaptic packing, and wiring minimisation scaling law, the arbours of all available neurons were split into axon and dendrite compartments. Then the dendritic sub-arbour was selected for further analysis, discarding the axonic compartment. For the cases of the first instar Drosophila larva (*14, 15, 76*), and adult mouse datasets (*17, 18*), existing expert annotations were used to split the neurons.

For ellipsoid body neurons, we computed the segregation index (SI), a measure of neuronal polarisation as established by (*42*). An SI of 1 indicates total segregation of inputs and outputs into dendrites and axon, respectively, while an SI of 0 indicates a homogeneous distribution. For neurones with a low segregation index (SI < 0.05), we considered the entire arbor as a dendritic tree as described in (*42*). Therefore, we treated these unsegregated neurons as purely dendritic, only removing the main trunk (linker segment) that stems from the soma of the rest of the analysis.

The remaining neurons from adult *Drosophila*, and larval zebrafish, were divided into axonic and dendritic compartments using a newly developed strategy that combines K-means clustering algorithms to find the nodes of the arbour that belong to the dendritic or axonic compartments, followed by consensus validation by 2 expert annotators (**Figure S5**).

Axon-dendrite split in the adult *Drosophila*. *Drosophila* neurons exhibit a diverse range of anatomical structures, reflective of their various functions within the insect's nervous system. However, a typical polarised neuron in *Drosophila* consists of a cell body (soma), from which an extended main branch connects a dendritic tree upstream, and axonal arbours downstream ((*77, 78*); **Figure S5A**). Our new algorithmic approach exploits those inherent differences in the structural characteristics of fly axons and dendrites to separate them effectively, applying the K-means clustering method to partition nodes of neuronal trees into axonal and dendritic compartments,(**Figure S5A**, step 1). The K-means clustering algorithm is a well-established

technique used for partitioning a dataset into K distinct, non-overlapping subsets (clusters). The algorithm identifies cluster centres (means) that minimise the within-cluster sum of squares (i.e., the Euclidean distance from each data point in the cluster to the mean).

Our strategy begins by representing each node in the neuronal tree as a 3d data point. Each dimension corresponds to a distinct coordinate of the node in space. Next, the K-means algorithm is applied to this 3-d dataset, with K set to 2, representing the two primary compartments of the neuron: the axon and the dendritic tree. The algorithm iteratively assigns each node to the cluster (compartment) whose mean is closest, then recomputes the means. This process is repeated until the assignment of nodes to clusters no longer changes. The choice of K as 2 is rooted in the biological structure of the neuron. Although there may be substructures within the axon and dendritic compartments that could be further subdivided, our aim was to initially segregate these two primary compartments (**Figure S5A**, step 2). Following the initial clustering that identifies two distinct compartments using our strategy, we make an anatomically informed assumption to further segregate the dendritic compartment. Given that the dendritic compartment is typically closer to the soma, we consider the cluster containing the soma node as the dendritic compartment in our first-pass analysis. Subsequently, we aim to further parse the dendritic compartment, removing the main branch nodes contained in the initial dendritic compartment. We compute the longest path length from the soma to the end of the arbour to identify the main branch, a criterion commonly used in computational neuroanatomy to identify the main branch (*64*). This is based on understanding that the main branch of a neuron does not constitute a significant part of the dendritic arbour and is typically longer than other branches (**Figure S5A**, step 3). The dendritic compartment is then redefined as the disjoint set of nodes found in the initial dendritic compartment minus the main branch. This method allows us to further refine our anatomical segregation of the neuron, allowing more detailed and granular analyses of the neuronal structure (**Figure S5A**, step43).

Axon-dendrite split in larva Zebrafish. In the case of zebrafish mitral cells, we slightly adapted our neuronal compartment K-mean clustering strategy to account for the unique morphology of these neurons (**Figure S5B**, step 1). The typical structure of an adult zebrafish mitral cell is characterised by a soma, from where a single primary dendrite terminating in dendritic tufts near the cell body, and a single axon projecting toward the medial or lateral olfactory tract (*91*). Although the approaches employed for the analysis of *Drosophila* neurons and zebrafish mitral cells share significant similarities, we leveraged unique features of the mitral cells to inform the axon-dendrite segregation. Since the Mitral cells' tufted dendritic structure is characterised by a high number of terminal points in comparison to the axonic region, we first define a rough dendritic compartment as the cluster yielded by the K-means method with the highest number of terminal points (**Figure S5B**, step 2). Refining the dendritic compartment in these cells presented additional challenges due to the occasional ambiguity in soma location from the reconstructions. To address this, we devised a new step in our method to identify the soma location. We identified the node from which all paths between the terminal nodes of the first-pass dendritic compartment heading towards the axon terminal converged as the soma location. This allowed us to segregate the dendritic compartment further, providing a more nuanced and detailed understanding of the unique structure of zebrafish mitral cells (**Figure S5,B**). Finally, to validate the efficacy of our approach, we validated our algorithm's classifications by a consensus analysis from 2 experts.

Finally, it is important to note that while our strategy offers a promising new approach for neuronal structure segmentation, there are a few limitations to consider. For example, the performance of the algorithm may be affected by the quality of the neuronal reconstructions and the choice of features used to represent each node. Furthermore, while we set K at 2 in this study, exploring different values of K could potentially provide more granular insights into neuronal architecture.

Dendritic synaptic density calculations

In this study, we quantified dendritic synaptic densities by determining the ratio of the total number of synapses within the dendrite to the corresponding total length of dendritic cable ($\frac{\#syn}{\mu m}$; **Table 5**). We measured the synaptic densities for all neurons in the species studied. For the *Drosophila* larva and mouse datasets, the detection of synapses was virtually complete, eliminating the need for further proofreading or adjustments. The comprehensive nature of these datasets ensured high precision in counting synaptic structures. For the other datasets, adult *Drosophila* and zebrafish, more detailed analysis or correction of synaptic counts was necessary to address artefacts associated with electron microscopy (EM) reconstructions. The approach for sorting or correcting the data was adapted based on the unique characteristics of each dataset.

For the adult *Drosophila* neurons, it was necessary to sort the data because the neuronal arbor reconstructions were incomplete. In particular, dendrites were often truncated (a false split), missing the small terminal synapse-bearing branches (the 'twigs' (*42*)), and therefore dendrites as provided present an over-representation of low-synapse density cable (the main shafts or 'backbone') in addition to potentially missing some synapses on the reconstructed cable. It is important to note the variability in reconstruction completion among neurons from different brain regions (**Figure S1C**). This is because the extent of proofreading varied across regions, leading to different estimates of missing synapses. Some regions, such as the central complex (*92*) and mushroom body (*93*), were extensively proofread due to their relevance in respective studies, while others were not.

To estimate the impact of these reconstruction errors on dendritic synaptic density, we use the fact that we know the amount of missing branches and synapses (the "postsynaptic completion rate" accessible via neuPrint `https://neuprint.janelia.org`, a tool for exploring connectomics datasets). After splitting the class-type morphologies into dendrites and axons

(see Section on distinguishing axons and dendritic compartments), we calculated the ratio of the number of synapses to the total dendritic cable ($\frac{\#syn}{\mu m}$) and compared it with the post-synaptic completion rate of the corresponding brain region. We found that the two quantities were correlated ($r = 0.61, p = 0$; **Figure S1C**). As a conservative measure to avoid biases in our analysis, we discarded all neurons in brain regions with a postsynaptic completion rate below 80%, using only neurons that satisfied this constraint in our analysis. For these neurons, no further processing was performed. It is important to note that no brain region had a completion rate greater than 90%, which could potentially reduce the density values of the neurons analysed (**Table 5**).

For zebrafish, we developed a different approach to correcting artefacts in neuronal arbour reconstruction and synapse annotation that impacted dendritic synaptic density measurement. During the reconstruction and proofreading of larval zebrafish neurons, certain biases were observed, which were attributed to the tracing and proofreading method employed in (*16*). Specifically, arbour tracing began at the soma rather than at the synapses, leading to sparser reconstructions by an increased number of errors of omission (starting from the synapses would have provided more points of cable convergence onto a neuronal arbour). This bias was exacerbated by the application of the redundant skeleton consensus procedure (RESCOP; (*94*)). That is, multiple individuals reconstructed the same arbour, and then only the common subset of the traced cable was retained as a means to minimise reconstruction errors. Given that in dendrites, most errors are of omission and overwhelmingly impact thin calibre synapse-bearing terminal cable, the application of RESCOP in all likelihood removed a substantial number of terminal cable and its synapses from the resulting consensus arbors. Not only was the total number of synapses reduced, but also resulted in an over-representation of dendritic shafts, which are cables of known low synaptic density.

In order to address these biases and towards estimating the real dendritic synaptic density, and given that unlike for the fly, the real distribution of synapses on dendritic cable is not known

for zebrafish, we implemented a simple scaling strategy for synaptic counts. The rationale is the following. Given that RESCOP crops terminal branches, we added one synapse to each terminal branch as a conservative measure. Conservative, because we expect each terminal branch to contribute little additional cable, but one or more synapses. This adjustment aimed to compensate for the likely under-representation of synapses on short, high-synapse-density terminal dendritic branches. We acknowledge that this is a rough approximation, but everything we know about dendritic arbors suggests that it is a lower bound approximation leading to an underestimation of the real dendritic synaptic density (**Table 5**).

Dendritic synaptic density invariance and rate code homeostasis

Recent theoretical work, reported in (*27*), demonstrates that the excitability of neurons that receive distributed synaptic input remains largely invariant despite variations in size and morphology. Neurons typically receive synaptic contacts across their dendritic tree. These dendrites, acting as leaky conductors, allow currents to propagate along dendritic cables towards the integration site. During the same time, these afferent currents leak across the cell membrane (*95*).

As dendrites increase in size, they can potentially form more synaptic connections, facilitating greater depolarisation due to increased afferent currents (*52, 67*). However, larger cells generally exhibit lower input resistances due to their increased length and membrane surface area, necessitating larger synaptic currents to achieve the same voltage response and bring a neuron to threshold (*52, 67*). (*27*) showed theoretically that these opposing phenomena cancel each other exactly for any dendritic morphology if the dendritic synaptic density is kept constant.

This homeostatic effect ensures that, for a given synaptic density, neuronal responses are determined solely by the average diameter of the dendritic and intrinsic conductivity. (*27*). This relationship holds across a wide range of morphologies, regardless of their arborisation com-

plexity, with the number of spikes closely approximating the input fraction of active synapses. This consistency occurs not only when synapses are uniformly activated but also when they are activated in clusters within a specific dendritic tree. Consequently, a neuron's firing rate homeostasis is largely dependent on synaptic density, highlighting the link between synaptic density invariance and functional stability.

Dendritic radius is tightly regulated across cell types and species due to factors such as volume conservation and conduction delays (*52, 62*). Despite this regulation, there are small variations (*27, 43, 52*). We hypothesised that small fluctuations, which could increase or decrease the input resistance, could be counteracted by adjustments in synaptic density around the observed mean of $\frac{1\text{syn}}{\mu\text{m}}$, or by variations in synaptic strength. Therefore, our objective was to identify correlations between these variables, providing evidence that changes in synaptic strength and density could serve as additional compensatory mechanisms to maintain firing rate homeostasis. In fact, within the mouse dataset, variations in dendritic radii are accompanied by corresponding adjustments in synaptic density around the mean of $\frac{1\text{syn}}{\mu\text{m}}$ ($r = 0.67, p = 0$; **Figure 2A**). Across different species, variations in the average dendritic radius are matched by increases in synaptic strength (measured by PSDs as a proxy) $r = 0.88, p = 0$; **Figure 2B**).

After identifying these relationships, we speculated that similar compensatory mechanisms could counterbalance differences in intrinsic conductivity between species (*27*). Although electrophysiological variables fall outside the scope of the anatomical datasets analysed in this study, recent studies suggest the existence of these mechanisms. Neurons are equipped with several compensatory strategies to maintain firing-rate homeostasis through adjustments in membrane conductance (*49, 50*). For example, in various species, excitable cells preserve their physiological properties despite substantial variations in physical size (*49*). Recent theoretical work shows that this can be compensated for by a mechanism that regulates multiple conductances (*49*). From an evolutionary perspective, there is experimental evidence that dif-

ferent species adjust neuronal properties to conserve how single neurons process information. In particular, species with thicker neurons, which exhibit higher membrane ionic conductances, maintain a conserved conductance per unit volume of the brain (*50*). Collectively, these findings suggest a consistent biophysical mechanism that influences intrinsic conductivity and contributes to the stability of neuronal activity despite variations in scale and connectivity across cell types and species.

It should be noted that, unlike the spike rate, invariance of synaptic density affords spike-time modulation through various factors (*27*). These include ion channel composition, cell-intrinsic properties, and morphology, which collectively contribute to enhancing neuronal computations (*27, 67*). Interestingly, recent research highlights the importance of maintaining the spike rate at a set point for reliable spike-time-dependent computations (*66*). Such mechanisms underscore the critical relationship between spike rate regulation and the computational reliability of spike timing-dependent plasticity and computations.

Dendritic inter-synaptic distance calculations

In our analysis, we computed the inter-synaptic distance by calculating the spatial locations of all synapses located along the paths extending from every terminal node leading to the dendritic root. Starting from the longest path to the root, we sequentially progressed through the longer paths until they reached the soma, or converged with a larger path length, at which point we transitioned to the next remaining longer path. The inter-synaptic distance was defined as the path length that stretches between one synapse and its immediate successor in the direction towards the dendritic root (**Table 4, 5**). In the context of the zebrafish dataset, a simple correction was implemented. Reconstruction and proofreading biases inherent in the dataset can induce omission errors in synapse-dense regions, particularly within smaller terminal branches, potentially skewing the distance distribution towards larger values. Thus, the inter-synaptic

distance for zebrafish was determined as described above, and then the length was adjusted proportionally based on the corrected count of corrected synapses (**Figure S1B**; see section on dendritic synaptic density calculations). This adjustment provides a closer estimation to the true inter-synaptic distance.

In general, this analysis was prompted by the hypothesis that although the density of the synaptic may be consistent between species, variations in the location of the synapse could significantly affect neuronal excitability. However, our analysis reveals that the inter-synaptic distance remains relatively constant across species, with *Drosophila* larva mean = $1.31\mu m \pm 0.49$; *Drosophila* adult mean = $1.89\mu m \pm 0.51$; zebrafish mean = $1.23\mu m \pm 0.47$ (uncorrected zebrafish inter-synaptic distance $= \frac{3.47syn}{\mu m} \pm 2.18$); mouse mean = $1.57\mu m \pm 0.45$ (**Table 5**).

Normalised Metric for Synapse Spatial Distribution

The spatial distribution of synapses on dendritic trees can influence the integration properties of neurons (*67*). A non-uniform distribution, characterised by clusters of synapses located distally or proximally, can affect the way a neuron processes and integrates incoming signals. To analyse the synapse spatial distribution, we introduced a relative metric that evaluates the position of synapses regardless of dendritic morphology. It quantifies the relationship between the average path length (PL) of the observed synapses and the expected PL distribution across a dendritic arbor, assuming a uniform random spatial distribution of synapses. In essence, the anatomical synapse locations are compared with the expected distribution of randomly sampled locations across all potential anatomical sites, specifically the nodes, within a given dendritic arbor. Here, the path length denotes the distance from a specific location in the dendritic tree to the root of the dendrite.

This metric provides a relative quantity, comparing the average observed synapse locations against the mean PL distribution of dendritic nodes after being sampled uniformly at random.

In order to compare across different cell-types and species, we bound the measure between 0-1, based on the shortest (proximal - 0) and longest (distal - 1) PLs in a given dendritic tree, with 0.5 being the mean PL of dendritic nodes when sampled uniformly at random. Through this, we can determine whether the synapses are located primarily proximally or distally from the root compared to the typical spatial distribution of the dendritic nodes.

Overall Synapse Distribution Metric: The overall synapse distribution metric quantifies how the average PL of observed synapse location compares to the distribution of node PLs in the dendritic tree. The metric is computed as follows:

1. **Calculate the mean PL of observed synapses** (N):

$$\bar{PL}_{\text{synapses}} = \frac{1}{N}\sum_{i=1}^{N} pl_i$$

2. **Determine the bounds for normalization**: Let D represent the dataset of all dendritic nodes' PL:

$$D = \{pl_1, pl_2, \ldots, pl_M\}$$

where M is the total number of nodes in the dendritic tree.

- *Lower bound* ($\bar{PL}_{min}$): mean PL of the shortest N dendritic nodes in D.
- *Upper bound* ($\bar{PL}_{max}$): mean PL of the longest N dendritic nodes in D.

3. **Calculate the mean PL after random sampling**: Given D, we aim to compute the average PL from random samples. For each iteration i (with $i = 1, 2, \ldots, 10000$), we randomly sample N nodes from D and compute the average PL for that sample:

$$\bar{PL}_i = \frac{1}{N}\sum_{j=1}^{N} pl_{\text{random}_j}$$

where pl_{random_j} is the jth randomly sampled path length from D in the ith iteration.

Finally, after completing all 10000 iterations, we compute the overall average:

$$\bar{PL}_{\text{overall}} = \frac{1}{10000} \sum_{i=1}^{10000} \bar{PL}_i$$

This $\bar{Pl}_{\text{overall}}$ represents the average PL computed from 10000 random samples of N nodes each from the dataset D.

4. **Create a Mapping Function**: We used either linear interpolation or direct linear functions to compute normalised values based on given data points. Both methods establish a linear relationship between known points. The value we sought to map was the mean path length ($\bar{PL}_{\text{synapses}}$) of observed synapses. By employing these techniques, we ensured that all values fall within the interval $[0, 1]$. Specifically, the randomly sampled mean serves as the breakpoint, mapping $\bar{PL}_{\text{overall}}$ to 0.5. Additionally, the lower bound $\bar{PL}_{min}$ maps to 0, and the upper bound $\bar{PL}_{max}$ maps to 1. This approach results in a continuous and monotonic transformation, enabling a normalised comparison of synapse distribution within the neuron's structure and facilitating comparison across different morphologies.

It is important to note that, while our methods provide a robust and interpretable framework for analysing the spatial distribution of synapses in neurons with varying morphological characteristics, it is crucial to address specific dataset limitations. For the neurons of adult *Drosophila* included in our study, there exists a potential for under-sampling, as we have a small sample ($N = 60$). In the zebrafish dataset, reconstruction and proofreading biases can cause omission errors in synapse-rich areas, especially smaller terminal branches, potentially skewing our analysis towards a more proximal distribution. In fact, in our data, we observed that the spatial location of the mean synapse of the zebrafish is more skewed to the proximal locations. (*D.*

larva mean = 0.55 ± 0.2; *D.* adult mean = 0.39 ± 0.12; zebrafish mean = 0.32 ± 0.15; mouse mean = 0.43 ± 0.2;**Table 4**; see **Table 5** for the datasets used).

Analysis of variability in synaptic density

We investigated the variability around the average synaptic density of $\frac{1\text{syn}}{\mu m}$ in dendrites of different species. We quantified additional anatomical variables that are known to influence cell excitability from electron microscopy (EM) datasets. Specifically, we measured the synaptic size and the radii of dendritic branches. However, not all EM datasets yielded all required morphometrics. Therefore, we supplemented the raddi values of the EM datasets with data from the light microscopy (LM) datasets (**Table 5**).

To correlate synaptic density with dendritic radii, we used mouse data sets (MICrONS cortical mm^3 and layer 2/3; **Table 1**; (*17, 18*)). These were the only datasets that allowed us to determine both radii and synaptic densities in all morphologies. Due to potential discrepancies introduced by different staining methods in mouse datasets (*96*)), which could affect cable volume measurements, we normalised the radii data for each mouse dataset.

Finally, we correlated dendritic radii with synaptic size using four EM datasets: *Drosophila* larva (*78*), adult *Drosophila* (*77, 92*), and mouse (*17, 18*) (see **Table 1**); and two LM datasets: rat (*84*) and human (*83*) (see **Table 2**). To measure postsynaptic density areas, we used five EM datasets: *Drosophila* larva (*78*), adult *Drosophila* (*88*), mouse (*53*), and human (*87*) (see **Table 3**).

Estimation of dendritic cable density range and volume conservation

This section expands on the insights proposed by Chklovskii et al. in (*62*). The authors hypothesised that evolution has fine-tuned neural circuits to minimise conduction delays, reduce dendrite attenuation, and use wiring cable efficiently. Through analytical methods, they demon-

strated that optimally wired neuronal circuits should allocate around "$\frac{3}{5}$" of its volume to axons and dendrites. They further proposed that the synaptic volume in the cortex, which is influenced by the number and size of synapses, must be regulated to preserve the "$\frac{3}{5}$" ratio. Consequently, we sought to explore whether the principle of volume conservation imposes constraints on dendritic synaptic density and to examine the ramifications on dendritic synaptic density. The main challenge was limited access to complete neuronal reconstructions and synapse sizes for the same neurons. However, for MICrONS cortical mouse data mm_3 (*18*), analysis was possible since the synaptic sizes were quantified (in arbitrary volume units based on the voxel sizes of the EM volume) in all available cells (**Table 4**).

Following (*62*), we assumed that cortical circuits are optimally packed and investigated how dendritic synaptic density would change if the total volume of synapses was spread among many small synapses versus a few larger ones. To do so, for each neuron in the dataset, we calculated the total volume occupied by its synapses. We then split the synaptic size distribution from each neuron into cumulative intervals ranging from 5% to 100% in steps of 5%, starting from the largest side of the distribution or the smallest. We then calculated the average synaptic sizes in the intervals. Subsequently, to determine the new values of dendritic synaptic density, we distributed the total synaptic volume over the synapses of size calculated in a given interval, yielding a new number of total potential synapses. We then adjusted the density of the dendritic cable synapse accordingly and calculated the total density in all neurons (**Figure S3A, B**).

Testing wiring minimisation scaling law

To challenge the wire minimisation properties of dendritic trees in our dataset ($N = 2486$; **Table 4** for the datasets used), we verified if the total length of the dendrite (L), the number of dendrite synapses (n) and the volume (V) were in accordance with the scaling law, $L \approx \sqrt[3]{\frac{3}{4*\pi}} \cdot \sqrt[3]{V} \cdot n^{\frac{2}{3}}$, as proposed by (*63*) (**Figure 1A**). The aforementioned morphome-

tics were computed using built-in functions from the TREES Toolbox (MATLAB; `https://www.treestoolbox.org`). To address issues in defining boundaries for large mouse dendritic trees with multiple subregions, we calculated the volumes of dendritic sub-trees in mouse neurons separately. By computing the volumes of sub-regions like apical and basal dendrites independently, we avoided potential volume overestimation. The total dendritic volume was the sum of these separate sub-tree volumes. Finally, to test the agreement between observed and predicted dendritic lengths, we performed a Pearson correlation analysis, comparing the real dendrite lengths (L_{Real}) from our data with the predicted lengths ($L_{Predicted}$) given the number of synapses and dendritic volumes .

To strengthen the robustness of our findings, we performed a sensitivity analysis in which we varied the number of synapses (n) in all morphologies to modulate synaptic dendritic density $\frac{\#syn}{\mu m}$ while maintaining length (L) and volume (V). Synapse densities increased by $\frac{0.1syn}{\mu m}$ steps, in a range between $\frac{[0.1-3]syn}{\mu m}$. This range was motivated by the lower and upper limits of the synaptic densities observed in the real data (minimal observed density $= \frac{0.259syn}{\mu m}$, maximum observed density $= \frac{2.95syn}{\mu m}$). We then calculated the theoretical lengths for all morphologies as a result of the varied synaptic. The synapse density that best matched wire minimisation predictions was identified by calculating the Euclidean distance between the vector of theoretical lengths for varied densities and the vector for real synapse counts and volumes. The density corresponding to the minimum distance provided the best agreement.

Statistical analysis

Statistical analyses were performed using Navis (Python), Natverve (R) and TREES Toolbox (Matlab). We used Pearson correlation and Spearman rank correlation to analyse the relationships between various parameters in our datasets. Permutation tests were used to quantify significance levels. The number of observations, significance values, and other relevant informa-

tion for data comparisons are specified in the respective figure legend and below. In all figures, * represents p value < 0.05, ** represents p value < 0.01, and *** represents p value < 0.001.

References and Notes

1. T. McMahon, J. T. Bonner, *On life and size* (Scientific American Books, New York, 1983).

2. A. Tzur, R. Kafri, V. S. LeBleu, G. Lahav, M. W. Kirschner, *Science* **325**, 167 (2009). ISBN: 1095-9203 (Electronic).

3. K. Shimono, *et al.*, *Scientific Reports* **4**, 4415 (2014).

4. P. Y. Wang, Y. Sun, R. Axel, L. Abbott, G. R. Yang, *Neuron* **109**, 3879 (2021).

5. H. Peng, *et al.*, *Nature* **598**, 174 (2021).

6. S. Herculano-Houzel, B. Mota, R. Lent, *Proceedings of the National Academy of Sciences* **103**, 12138 (2006).

7. S. Herculano-Houzel, C. E. Collins, P. Wong, J. H. Kaas, *Proceedings of the National Academy of Sciences* **104**, 3562 (2007).

8. K. Schmidt-Nielsen, *Scaling: why is animal size so important?* (Cambridge university press, Cambridge, United Kingdom, 1984).

9. K. Healy, L. McNally, G. D. Ruxton, N. Cooper, A. L. Jackson, *Animal Behaviour* **86**, 685 (2013).

10. K. Kverková, *et al.*, *Proceedings of the National Academy of Sciences* **119**, e2121624119 (2022).

11. S. Srinivasan, C. F. Stevens, *Current Biology* **29**, 2533 (2019). Publisher: Elsevier Ltd.

12. G. B. West, J. H. Brown, B. J. Enquist, *Science* **276**, 122 (1997). ISBN: 00368075̊10959203.

13. J. H. Brown, G. B. West, *Scaling in Biology* (Oxford University Press, Oxford, United Kingdom, 2000).

14. K. Eichler, *et al.*, *Nature* **548**, 175 (2017). Publisher: Nature Publishing Group.

15. M. Winding, *et al.*, The connectome of an insect brain, *preprint*, Neuroscience (2022).

16. A. A. Wanner, R. W. Friedrich, *Nature Neuroscience* **23**, 433 (2020). Publisher: Springer US.

17. MICrONS Consortium, *et al.*, Functional connectomics spanning multiple areas of mouse visual cortex, *preprint*, Neuroscience (2021).

18. C. M. Schneider-Mizell, *et al.*, Cell-type-specific inhibitory circuitry from a connectomic census of mouse visual cortex, *preprint*, Neuroscience (2023).

19. S. Loomba, *et al.*, *Science* p. eabo0924 (2022).

20. J. DeFelipe, *Cerebral Cortex* **9**, 722 (1999).

21. A. Santuy, *et al.*, *Scientific Reports* **10**, 14014 (2020).

22. F. Zhu, *et al.*, *Neuron* **99**, 781 (2018).

23. R. Benavides-Piccione, I. Ballesteros-Yáñez, J. DeFelipe, R. Yuste, *Journal of Neurocytology* **31**, 337 (2002).

24. P. Vanderhaeghen, F. Polleux, *Nature Reviews Neuroscience* **24**, 213 (2023).

25. M. London, M. Häusser, *Annual review of neuroscience* **28**, 503 (2005).

26. P. Poirazi, A. Papoutsi, *Nature Reviews Neuroscience* **21**, 303 (2020). Publisher: Springer US ISBN: 4158302003017.

27. H. Cuntz, *et al.*, *Neuron* pp. 1–16 (2021). Publisher: Elsevier Inc.

28. A. D. Bird, P. Jedlicka, H. Cuntz, *PLOS Computational Biology* **17**, e1009202 (2021).

29. S. Ioffe, C. Szegedy, Batch Normalization: Accelerating Deep Network Training by Reducing Internal Covariate Shift (2015). ArXiv:1502.03167 [cs].

30. T. Salimans, D. P. Kingma, Weight Normalization: A Simple Reparameterization to Accelerate Training of Deep Neural Networks (2016). ArXiv:1602.07868 [cs].

31. I. Goodfellow, Y. Bengio, A. Courville, *Deep learning* (MIT press, Cambridge, Massachusetts, 2016).

32. J. Schmidhuber, *Neural Networks* **61**, 85 (2015).

33. S. Gerhard, I. Andrade, R. D. Fetter, A. Cardona, C. M. Schneider-Mizell, *eLife* **6:e29089**, 1 (2017). ISBN: 2050-084X (Electronic) 2050-084X (Linking).

34. W. F. Tobin, R. I. Wilson, W. C. A. Lee, *eLife* **6**, 1 (2017).

35. P. Schlegel, *et al.*, *BioRxiv* (2023).

36. D. Witvliet, *et al.*, *bioRxiv* p. 2020.04.30.066209 (2020).

37. G. Gutiérrez-Ospina, *et al.*, *Brain, Behavior and Evolution* **64**, 61 (2004).

38. M. Ahmed, *et al.*, Hacking brain development to test models of sensory coding, *preprint*, Neuroscience (2023).

39. J. Valdes-Aleman, *et al.*, *Neuron* **109**, 105 (2021). Publisher: Elsevier Inc.

40. M. Tripodi, J. F. Evers, A. Mauss, M. Bate, M. Landgraf, *PLoS Biology* **6**, 2172 (2008).

41. E. L. Heckman, C. Q. Doe, *eLife* **11**, e82093 (2022).

42. C. M. Schneider-Mizell, *et al.*, *eLife* **5**, 1 (2016). ISBN: 10.1101/026617.

43. H. Cuntz, A. Borst, I. Segev, *Theoretical Biology and Medical Modelling* **4**, 1 (2007).

44. L. M. Yu, Y. Goda, *Current Opinion in Neurobiology* **19**, 327 (2009).

45. M. Schneider, *et al.*, *PLOS Computational Biology* **19**, e1011212 (2023).

46. G. H. Diering, *et al.*, *Science* **355**, 511 (2017).

47. L. Beaulieu-Laroche, *et al.*, *Cell* **175**, 643 (2018). Publisher: Elsevier Inc.

48. S. Aljaberi, T. O'Leary, F. Forni, *2021 European Control Conference (ECC)* (IEEE, 2021), pp. 306–311.

49. S. Gorur-Shandilya, E. Marder, T. O'Leary, *Scientific Reports* **10**, 15989 (2020).

50. L. Beaulieu-Laroche, *et al.*, *Nature* **600**, 274 (2021). Publisher: Springer US.

51. N. L. Turner, *et al.*, *Cell* pp. 1082–1100 (2022).

52. P. Sterling, S. Laughlin, *Principles of Neural Design* (MIT Press, Cambridge, Massachusetts, 2015).

53. S. Holler, G. Köstinger, K. A. Martin, G. F. Schuhknecht, K. J. Stratford, *Nature* **591** (2021). Publisher: Springer US.

54. A. Holtmaat, K. Svoboda, *Nature Reviews Neuroscience* **10**, 647 (2009).

55. T. E. Faust, G. Gunner, D. P. Schafer, *Nature Reviews Neuroscience* **22**, 657 (2021).

56. M. Germann, S. G. Brederoo, I. E. Sommer, *Current Opinion in Psychiatry* **34**, 222 (2021).

57. M. A. Chirillo, M. S. Waters, L. F. Lindsey, J. N. Bourne, K. M. Harris, *Scientific Reports* **9**, 3861 (2019).

58. A. R. Chambers, S. Rumpel, *Neuroscience* **357**, 172 (2017).

59. D. Meyer, T. Bonhoeffer, V. Scheuss, *Neuron* **82**, 430 (2014).

60. S. Royer, D. Paré, *Nature* **422**, 518 (2003).

61. J. N. Bourne, K. M. Harris, *Hippocampus* **21**, 354 (2011).

62. D. B. Chklovskii, T. Schikorski, C. F. Stevens, *Neuron* **34**, 341 (2002).

63. H. Cuntz, A. Mathy, M. Häusser, *Proceedings of the National Academy of Sciences* **109**, 11014 (2012).

64. A. Ferreira Castro, *et al.*, *eLife* **9**, e60920 (2020).

65. D. B. Chklovskii, *Neuron* **43**, 609 (2004).

66. M. Saponati, M. Vinck, *Nature Communications* **14**, 4985 (2023).

67. P. Dayan, L. F. Abbott, *Theoretical neuroscience: computational and mathematical modeling of neural systems* (MIT press, 2005).

68. M. London, A. Roth, L. Beeren, M. Häusser, P. E. Latham, *Nature* **466**, 123 (2010).

69. D. Beniaguev, I. Segev, M. London, *Neuron* **109**, 2727 (2021).

70. P. Poirazi, T. Brannon, B. W. Mel, *Neuron* **37**, 989 (2003).

71. A. Gidon, *et al.*, *Science* **367**, 83 (2020).

72. M. Larkum, *Neuroscience* (2022). Publisher: IBRO.

73. A. Tzilivaki, G. Kastellakis, P. Poirazi, *Nature Communications* **10**, 3664 (2019).

74. J. K. Lappalainen, *et al.*, *bioRxiv* pp. 2023–03 (2023).

75. B. A. Richards, *et al.*, *Nature Neuroscience* **22**, 1761 (2019). Publisher: Springer US.

76. T. Ohyama, *et al.*, *Nature* **520**, 633 (2015).

77. L. K. Sche, *et al.*, *eLife* **9**, e57443 (2020).

78. M. Winding, *et al.*, *Science* **379**, eadd9330 (2023).

79. G. A. Ascoli, D. E. Donohue, M. Halavi, *Journal of Neuroscience* **27**, 9247 (2007). ISBN: 2712005775.

80. S. Saalfeld, A. Cardona, V. Hartenstein, P. Tomancak, *Bioinformatics* **25**, 1984 (2009).

81. R. E. Horton, *Geological society of America bulletin* **56**, 275 (1945).

82. A. Stahler, *Geol Soc Am Bull* **63**, 1117 (1952).

83. C. Koch, A. Jones, *Neuron* **92**, 612 (2016).

84. N. Ishizuka, W. M. Cowan, D. G. Amaral, *Journal of Comparative Neurology* **362**, 17 (1995).

85. C. L. Barnes, D. Bonnéry, A. Cardona, *PLOS ONE* **17**, e0266064 (2022).

86. T. M. Bartol, *et al.*, *eLife* **4**, 1 (2015).

87. S. Plaza-Alonso, N. Cano-Astorga, J. DeFelipe, L. Alonso-Nanclares, Volume Electron Microscopy Reveals Unique Laminar Synaptic Characteristics in the Human Entorhinal Cortex (2023).

88. Z. Zheng, *et al.*, *Doi.Org* p. 140905 (2017).

89. H. Cuntz, F. Forstner, A. Borst, M. Häusser, *PLoS Computational Biology* **6** (2010). ISBN: 1553-7358 (Electronic)\r1553-734X (Linking).

90. A. S. Bates, *et al.*, *Current Biology* **30**, 3183 (2020). Publisher: Elsevier Ltd.

91. C. L. Fuller, H. K. Yettaw, C. A. Byrd, *The Journal of Comparative Neurology* **499**, 218 (2006).

92. B. K. Hulse, *et al.*, *eLife* **10**, e66039 (2021).

93. F. Li, *et al.*, *eLife* **9**, e62576 (2020).

94. M. Helmstaedter, K. L. Briggman, W. Denk, *Nature Neuroscience* **14**, 1081 (2011).

95. W. Rall, *Annals of the New York Academy of Sciences* **96**, 1071 (1962).

96. N. Korogod, C. C. Petersen, G. W. Knott, *eLife* **4**, e05793 (2015).

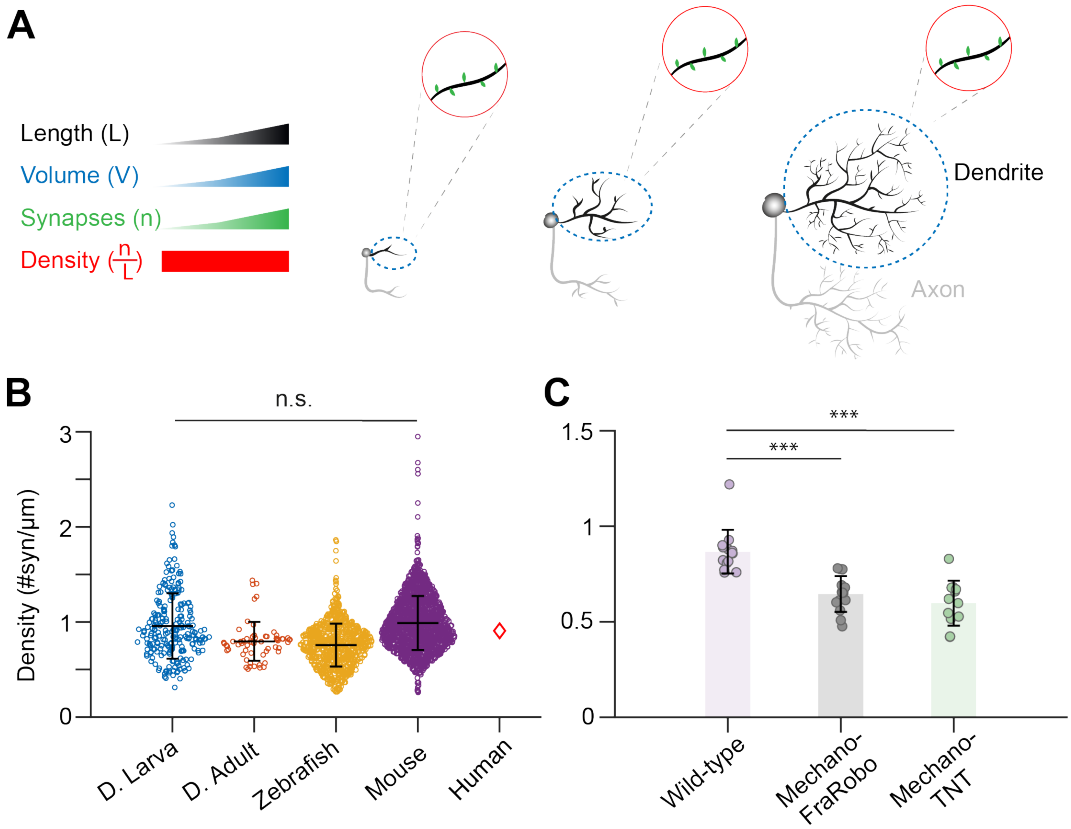

Figure 1: **Synaptic density comparisons across species and mutants**. **A**, Schematic of the quantities used throughout this study. Namely, dendritic length (L; black), volume (V; dashed blue ellipse), and number of synapses (n; green). Inset zooming in dendrite cable in red highlights that the dendritic synaptic density is constant regardless of cell size or complexity. Axon is depicted in gray and soma as the circular gray structure connecting dendrites and axons. **B**, Swarm plot of synaptic densities across species ($N_{Total} = 2486$, $N_{D.Larva} = 233$, $N_{D.Adult} = 60$, $N_{Zebrafish} = 709$, $N_{Mouse} = 1484$; see Table 1, 4 and Methods). Each data point is one neuron, with the colour corresponding to species. Horizontal black line indicates mean values per species; error bars, standard deviation. Red diamond shape indicates mean values of corresponding species from (*19*). Pair-wise statistical analysis using permutation tests, "n.s." non significant. **C**, Bar plot of synaptic densities across wild-type *Drosophila* larva mechanosensory neurons and mutants. On each plot, coloured bars corresponds to mean values, respectively per EM volume. Error bars indicate standard deviation ($N_{WT} = 14$, $N_{TNT} = 12$, $N_{FraRobo} = 14$; see Methods). Pair-wise statistical analysis using permutation tests, $***p < 0.001$.

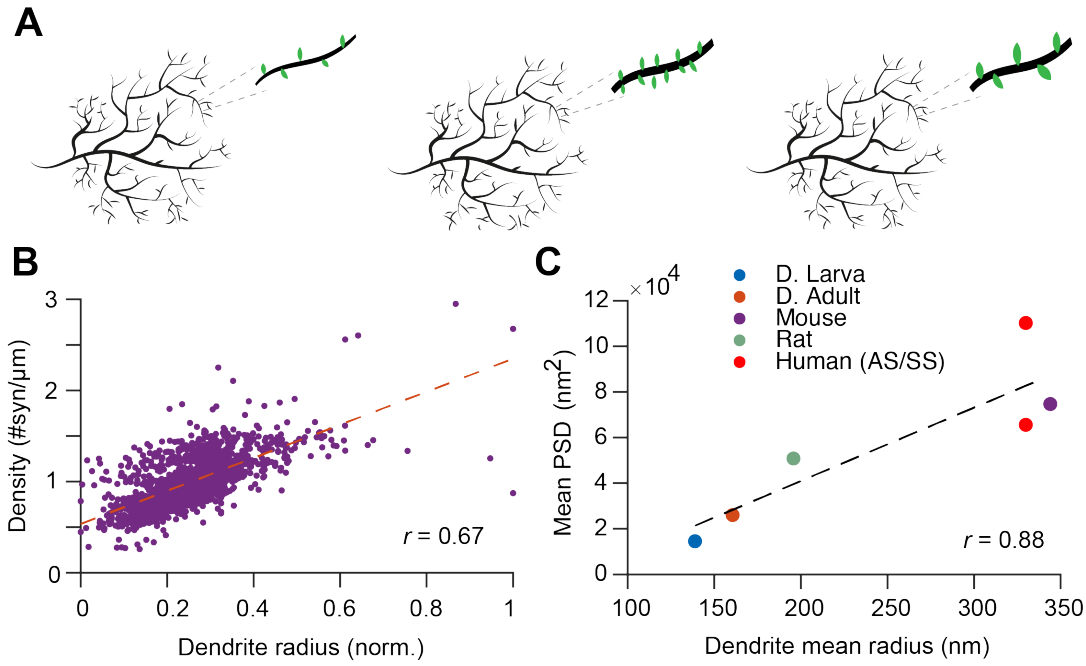

Figure 2: **Dendritic radius correlates with synaptic density and synapse size. A**, Schematic of compensatory mechanisms maintaining neuronal excitability. Left: dendrite (black) with invariant synaptic density (green synapses). Middle: thicker dendrite adjusts synaptic density to offset lower input resistance. Right: thicker dendrite with larger synapses to offset lower input resistance. **B**, Correlation plot of dendrite radius (normalised radius size data; $N = 1446$; see Methods) against dendrite synaptic density ($\frac{\#syn}{\mu m}$) in mouse cells (correlation coefficient of $r = 0.67, p = 0$). Data points represent individual cells, colours as before. The data are fit with a line of slope 1.81 ± 0.05 (orange dashed line) to assess the relationship between dendritic radius and synaptic density. **C**, Correlation plot between the mean radius of dendrites and the size of synapses, measured by the area of postsynaptic densities (PSDs), across different species (correlation coefficient of $r = 0.88, p = 0.018$). Each colour represents a different species (see Table 2, 3 and Methods). For human data, "AS" is asymmetric synapses (larger PSD value) and "SS" is symmetric synapse (smaller PSD value). The data are fit with a line of slope 321.25 ± 87.82 (black dashed line) to assess the relationship between dendritic radius and synaptic size (PSD). Correlation coefficients (r) were obtained using Pearson correlation, and p values obtained from a permutation test; lines were fit using linear regression.

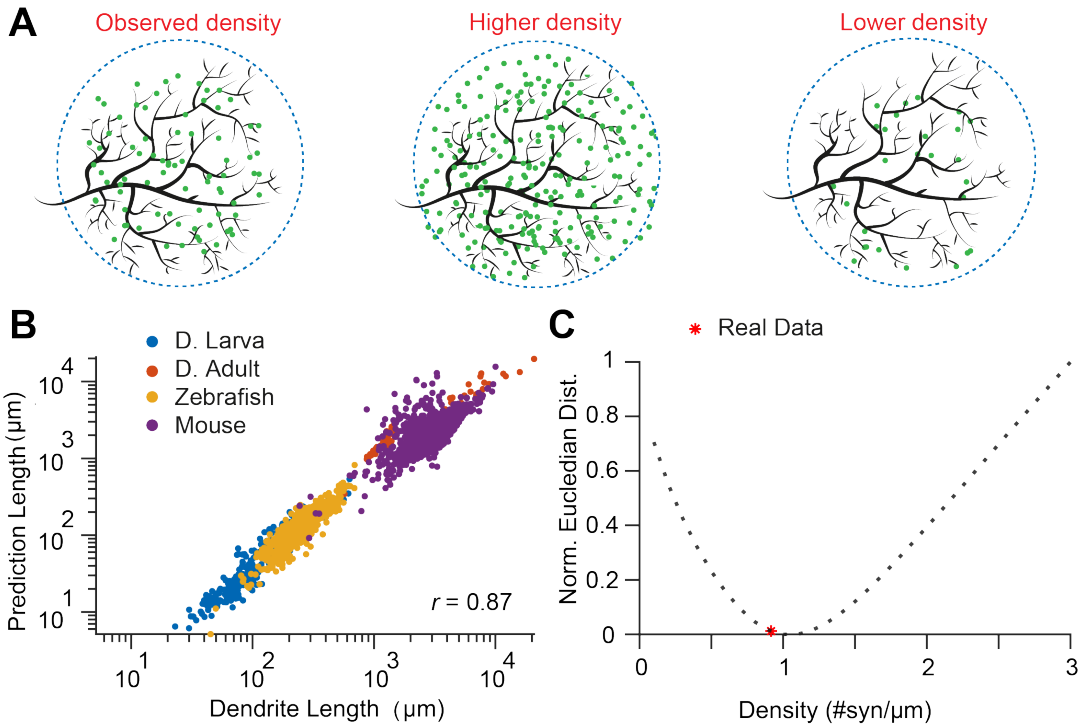

Figure 3: **Dendritic structure scaling relationships and synaptic density across species**. **A**, Schematic illustrating the impact on synaptic density by varying the number of synapses (green) while keeping dendritic length (black) and volume (blue dashed ellipse) constant. **B**, Shown is the relation between total dendrite length of real dendrites (L_{Real}) and the predicted length ($L_{Predicted}$) computed using the scaling law for all morphologies of all datasets besides human data ($N = 2486$; log-transformed data; see Table 1, 4). The predicted length strictly follows the equation in all species ($r = 0.86, p = 0$). Each datapoint is one neuron, with the colour corresponding to species, similar to **Figure 1B**. **B**, Sensitivity analysis of synaptic density and wiring optimisation. Plotting the normalised euclidean distance against synaptic density, resulting from changing the synaptic density of all morphologies while evaluating the distance between $L_{Predicted}$ vs. L_{Real} reveals that gains in wiring minimisation show an inflection point around $1syn/\mu m$. Red star sign denotes the measured mean synaptic density across datasets. Correlation coefficient (r) was obtained using Pearson correlation, and p values obtained from a permutation test.

Supplementary figures

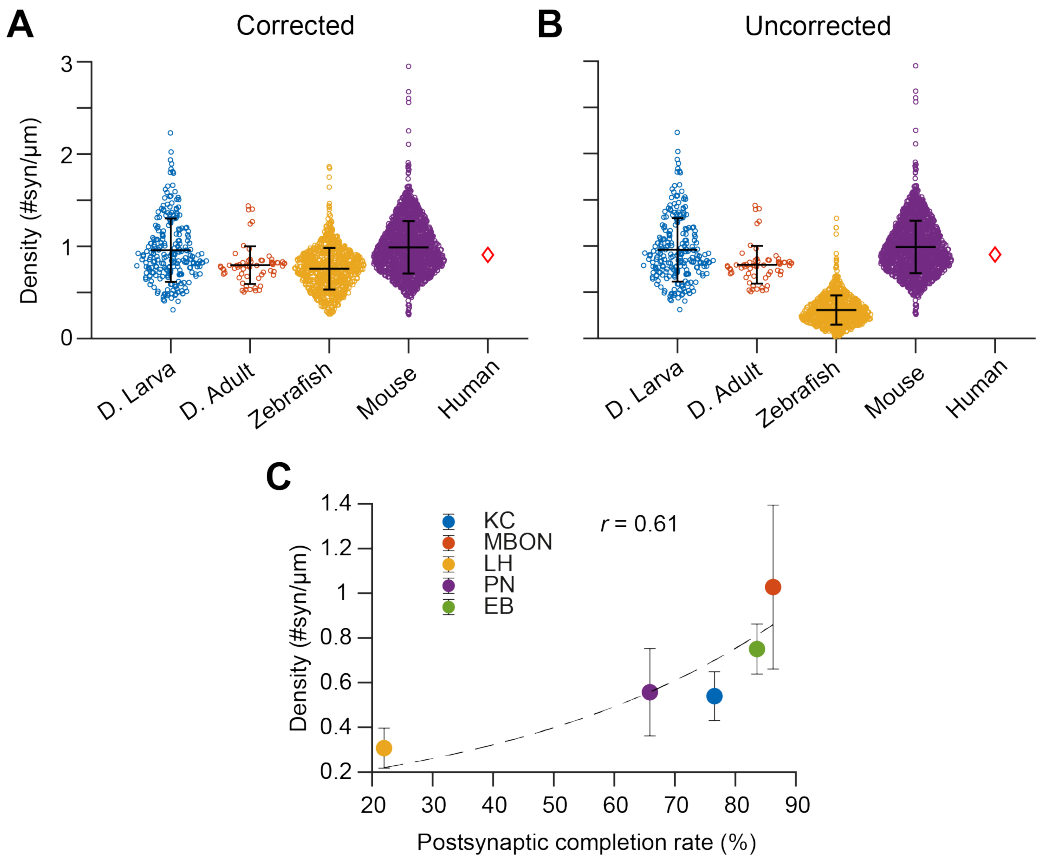

Figure S1: **Synaptic density corrections and correlation analysis with reconstruction level. A**, Same as **Figure 1B**. **B**, Similar swarm plot of synaptic densities across species as in **A**, but with uncorrected zebrafish density values (see Methods). **C**, Correlation plot showing dendritic synaptic density as a function of postsynaptic completion rate in the adult fly Hemibrain connectome ($r = -0.61, p = 0$; Table 1; see Methods) (*77, 92*). Different colours indicate different cell types in the adult fly brain. Error bars indicate the standard deviation. The data are fitted with an exponential fit (black dashed line) to assess the relationship between dendritic radius and synaptic density. The correlation coefficient (r) was obtained by Spearman's rank correlation, and p values were obtained from a permutation test.

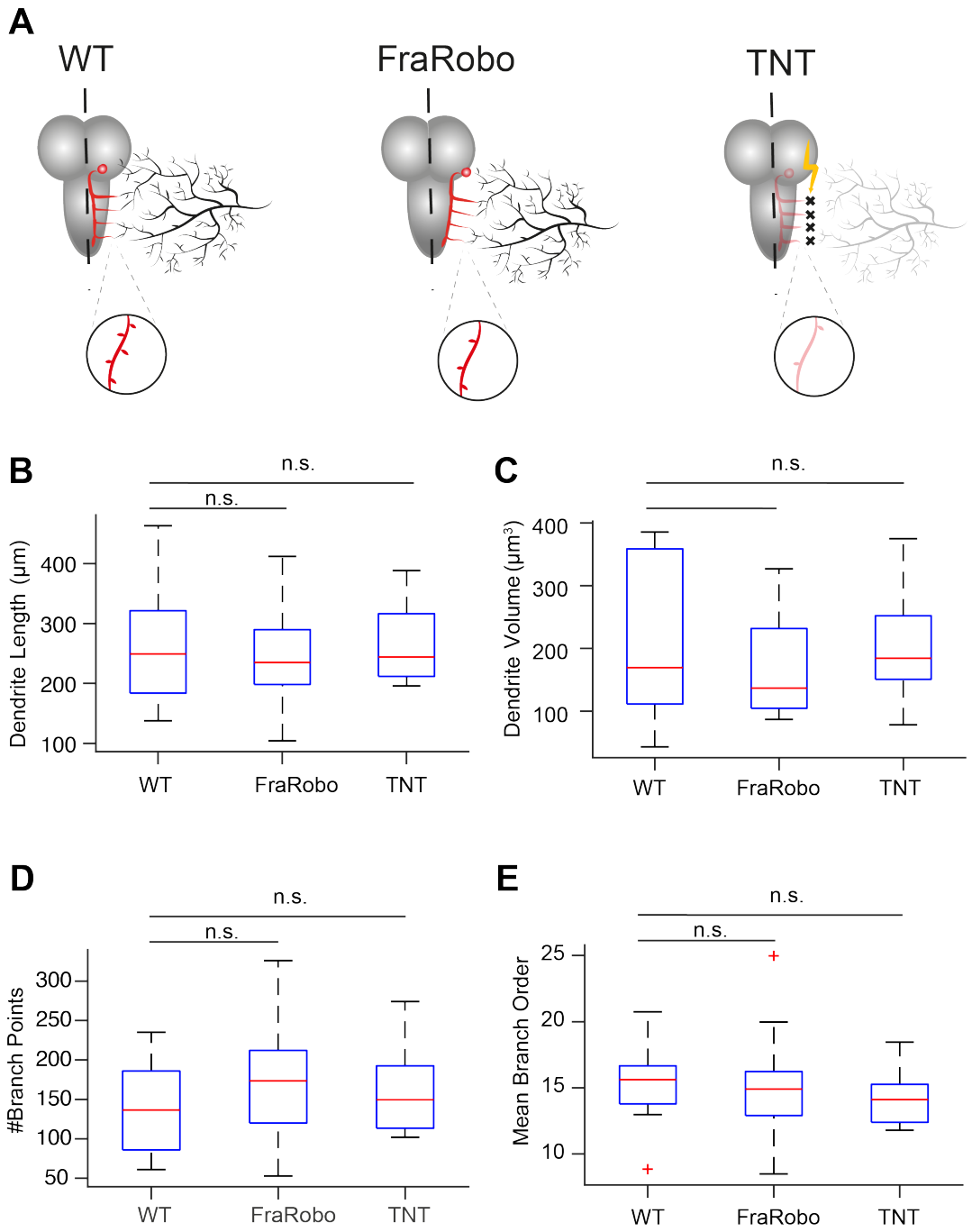

(Continues next page)

Figure S2: **Comparative analysis of dendritic morphometrics in WT, FraRobo, and TNT EM volumes A**, Schematic of EM volumes used in the comparative dendritic cable density analysis. Left scheme, wild-type: depicts the larval *Drosophila* brain and ventral nerve cord (grey) with a central dashed line indicating the body's axis of left-right symmetry. The mechanical sensory axon is shown in red, connecting to dendritic trees (black). The inset highlights synapse density. Central scheme, FraRobo mutant: similar to WT scheme, but with the mechanical sensory axon (red) shifted from its typical location. Right scheme, TNT mutant: illustrates the silencing of activity in the mechanical sensory axons. **B**, Box plot showing the distribution of dendritic length across wild type (WT; $N = 14$), FraRobo ($N = 14$), and TNT ($N = 14$) mutants. **C-E**, same as **A**, but for dendritic volume, number of branch points, and mean branch order measurements. The red plus symbols indicate outliers within the data set for each condition. Outliers were defined based on the interquartile range. Horizontal lines above the plots denote statistical comparisons, with "n.s." indicating a lack of statistical significance, with p values obtained from permutation tests.

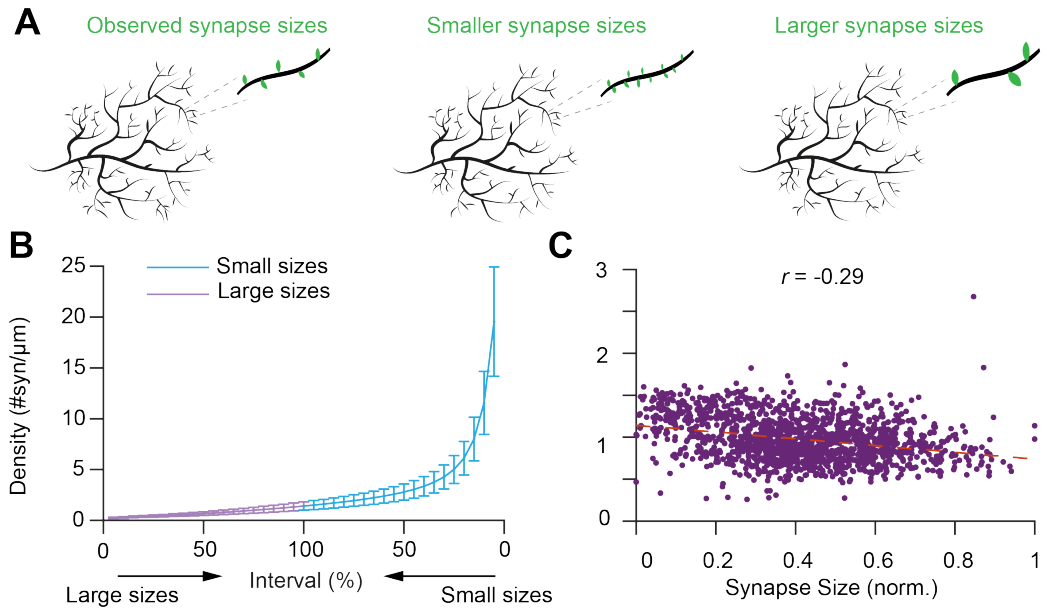

Figure S3: **Impact of synaptic size packing on dendritic synaptic density in mouse cells A**, The schematic illustrates how different synapse packing arrangements affect synaptic density, without changing the total synaptic volume (shown in green). This effect is observed as synapses are dispersed along a dendritic arbour (black) in the form of numerous smaller synapses or a reduced number of larger synapses. **B** Plot showing dendritic synaptic density computed by distributing synapses across mean sizes found in the observed size distribution intervals. The x-axis represents the cumulative intervals in percentage, computed in steps of 5% either starting from the larger 5% synapses or from the smaller 5% synapses. The y-axis shows the mean synaptic density for the values yielded by these intervals. Different colours indicate separate starting points for interval computation. Error bars indicate standard deviation. **C**, Correlation plot of mean dendritic synapse size (normalised data; $N = 1183$ from (*18*); see Methods) against dendrite synaptic density ($\frac{\#syn}{\mu m}$) in mouse cells (correlation coefficient of $r = -0.29, p = 0$). Data points represent individual cells, colours as before. The data are fit with a line of slope -0.4 ± 0.04 (orange dashed line) to assess the relationship between dendritic radius and synaptic density. Correlation coefficient (r) was obtained by Pearson correlation, and p values were obtained from a permutation test; lines were fit using linear regression.

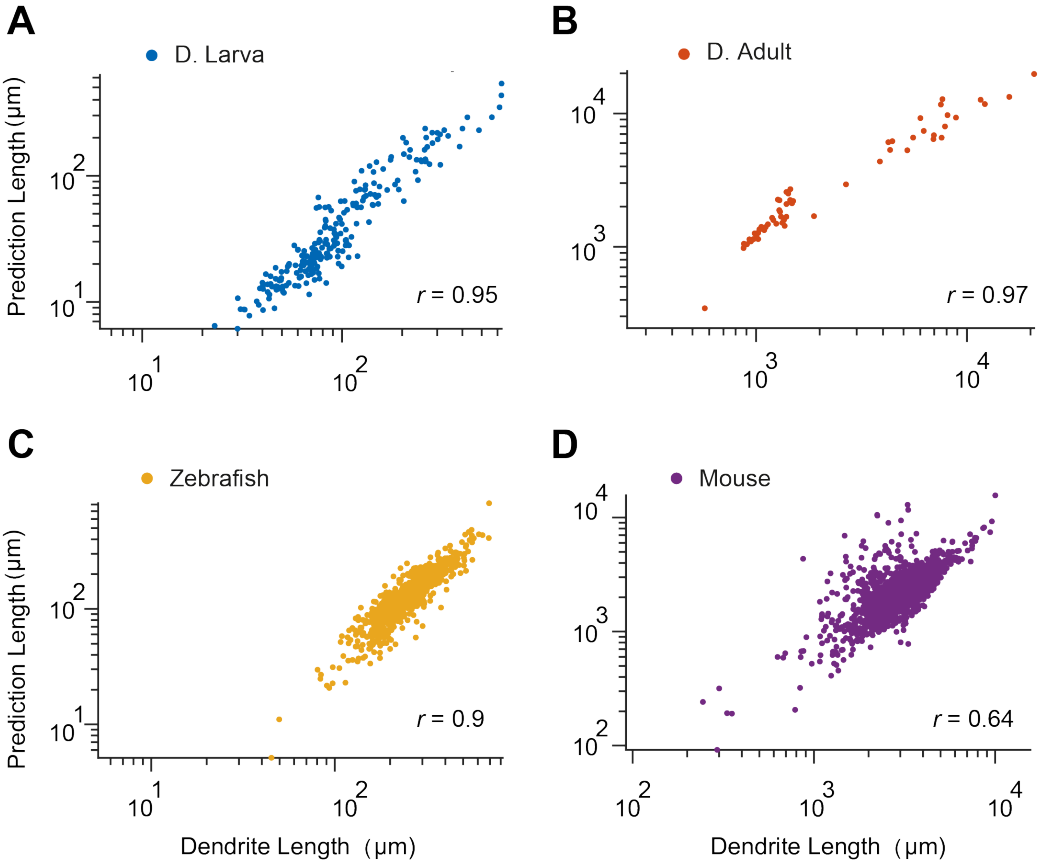

Figure S4: **Scaling relationships plotted across individual species. The data is the same as in Figure 1C**. **A**, Shown is the relation between total dendrite length of real dendrites (L_{Real}) and the predicted length ($L_{Predicted}$) computed using the scaling law for all *Drosophila* larva morphologies ($N = 233$; $r = 0.95$, $p = 0$; log-transformed data; Table 1). **B-D**, same as in **A** but for adult *Drosophila* ($N = 60$; $r = 0.94$, $p = 0$); larval zebrafish ($N = 709$; $r = 0.9$, $p = 0$); and mouse ($N = 1484$; $r = 0.64$, $p = 0$). Correlation coefficients (r) were obtained by Pearson correlation, and p values were obtained from a permutation tests.

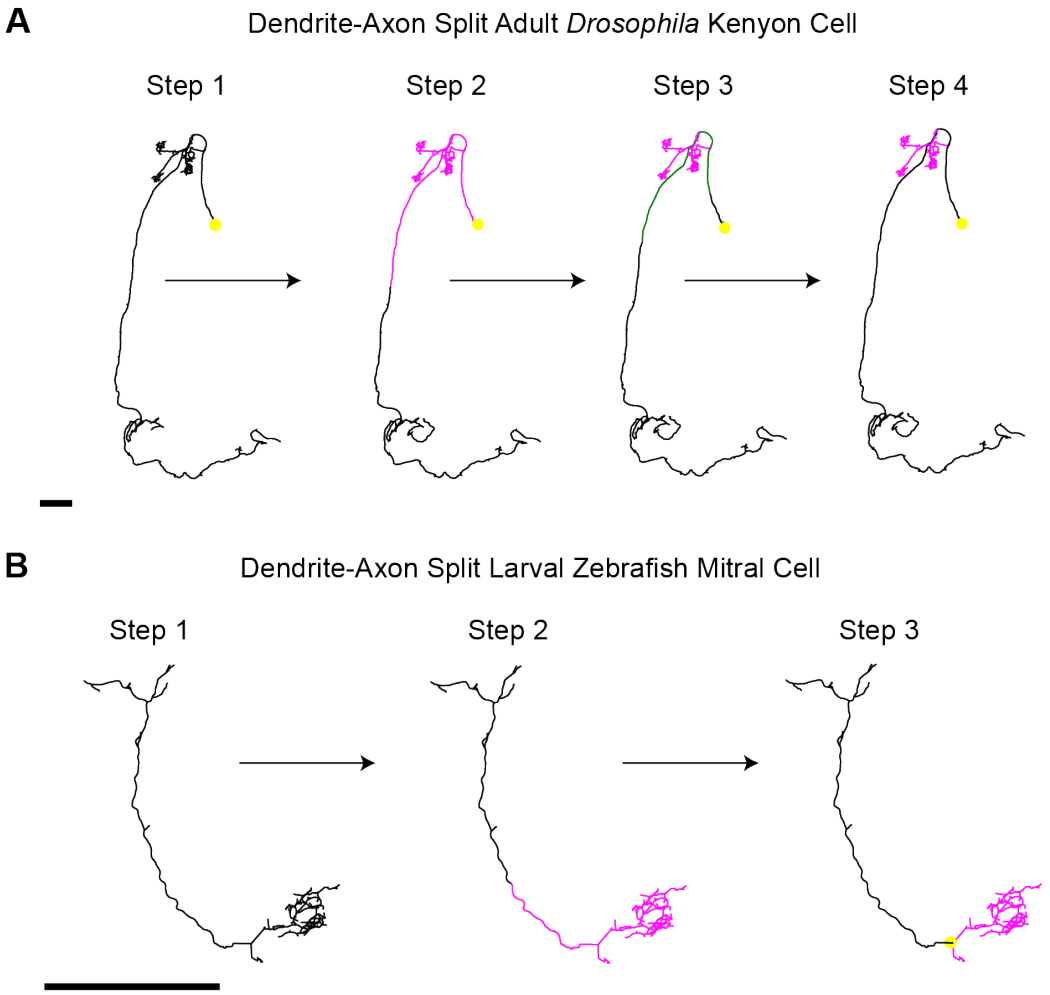

Figure S5: **Illustrative dendrite-axon split algorithm for adult *Drosophila* and zebrafish datasets.A**, Dendrite-axon split in adult *Drosophila* Kenyon-cell. The figure shows the four-step process: starting with the reconstructed morphology, then illustrating the separated compartments using K-means, highlighting the dendritic (pink) and axonal (black) and main trunk (green), and finally presenting the dendritic tree after main branch removal, with the soma marked (yellow dot). **B**, Dendrite-axon split of larval zebrafish mitral cell. The three-step process starts with representative morphology, then shows separated compartments (dendritic in pink and axonal in black) using K-means, and finally highlights the dendritic compartment (pink) and the soma proxy location (yellow). Scale bars: 10 μm.

Tables

Cell-types details derived from electron microscopy				
Cell-type (brain region)	**Species**	**Sample Size**	**Sex**	**Age**
Kenyon-Cell (*14, 78*)	Larval (L1) *D.Melanogaster*	150	F	L1
Projection Neuron (*14, 78*)	Larval (L1) *D.Melanogaster*	43	F	L1
Mushroom Body Output Neuron (*14, 78*)	Larval (L1) *D.Melanogaster*	40	F	L1
Basin (*39, 76*)	Larval (L1) *D.Melanogaster*	8	F	L1
Griddle (*39, 76*)	Larval (L1) *D.Melanogaster*	2	F	L1
Drunken (*39, 76*)	Larval (L1) *D.Melanogaster*	4	F	L1
Basin (*39*)	*FraRobo* Larval (L1) *D.Melanogaster*	8	F	L1
Griddle (*39*)	*FraRobo* Larval (L1) *D.Melanogaster*	2	F	L1
Drunken (*39*)	*FraRobo* Larval (L1) *D.Melanogaster*	4	F	L1
Basin (*39*)	*TNT* Larval (L1) *D.Melanogaster*	8	F	L1
Griddle (*39*)	*TNT* Larval (L1) *D.Melanogaster*	2	F	L1
Drunken (*39*)	*TNT* Larval (L1) *D.Melanogaster*	2	F	L1
Kenyon-Cell (*77*)	Adult *D.Melanogaster*	282	F	few hrs after pupa
Projection Neuron (*77*)	Adult *D.Melanogaster*	52	F	few hrs after pupa
Mushroom Body Output Neuron (*77*)	Adult *D.Melanogaster*	10	F	few hrs after pupa
Lateral Horn Neuron (*77*)	Adult *D.Melanogaster*	73	F	few hrs after pupa
Ellipsoid body (*92*)	Adult *D.Melanogaster*	50	F	few hrs after pupa
Mitral Cells (*77*)	Zebrafish larva	709	M & F	4-5d AEF
Visual Cortex Layer 2/3 pyramidal cell (*17*)	Mouse	649	M	P36
Visual Cortex Layer 4 pyramidal cell (*18*)	Mouse	263	M	P36
Visual Cortex Intratelencephalic-projecting Layer 5 pyramidal cell (*18*)	Mouse	137	M	P36
Visual Cortex Near-projecting Layer 5 pyramidal cell (*18*)	Mouse	10	M	P36
Visual Cortex Extratelencphalic-projecting Layer 5 pyramidal cell (*18*)	Mouse	37	M	P36
Visual Cortex Corticothalamic-projecting Layer 6 pyramidal cell (*18*)	Mouse	143	M	P36
Visual Cortex Intratelencephalic-projecting Layer 6 pyramidal cell (*18*)	Mouse	192	M	P36
Visual Cortex uncertain Layer 6 pyramidal cell (*18*)	Mouse	28	M	P36
Visual Cortex unsure cell type (*18*)	Mouse	5	M	P36
Visual Cortex White matter adjacent layer 6b pyramidal cell (*18*)	Mouse	20	M	P36
Superior Temporal Gyrus* (*19*)	Human	n=2 datasets	M & F	80y; 69y

Table 1: **Details of species, brain regions and cell-types used in this study stemming from electronic microscopy.**
The table provides a comprehensive overview of the cell-types investigated across various species, including *Drosophila* (both larval and adult stages), zebrafish, mouse, and human. For each cell-type, the corresponding species, sample size, sex, and age are listed. Sex is Female (F), Male (M). Age is hours after egg laying (AEL), hours after pupating, post embryonic days (P_{days}), or human subjects age years (y). Star sign denotes datasets from which estimations of synaptic density were retrieved, but anatomical data were not available. References for the data sources are provided.

Cell-types details derived from light microscopy				
Cell-type	**Species**	**Sample Size**	**Sex**	**Age**
Hippocampus Pyramidal Cell (*84*)	Rat	47	F	P33-P57
Neocortical Layer 3 Aspiny cell (*83*)	Human	21	F	27y
Neocortical Layer 3 Spiny cell (*83*)	Human	31	F	27y
Neocortical Layer 3 Pyramidal Cell (*83*)	Human	80	F	27y

Table 2: **Details of species, brain regions and cell-types of used in this study stemming form light microscopy.**
The table provides an overview of the cell-types investigated across different species using light microscopy. The specific brain regions, sample sizes, sex, and age of the subjects are detailed. Sex is Female (F), Male (M). Age is post embryonic days (P_{days}), or human subjects age years (y). References for the data sources are provided.

Postsynaptic density details derived from electronic microscopy				
Species	**Brain region**	**Sample size**	**Mean area (nm^2)**	**Neurotransmitter type**
Drosophila larva (*85*)	Antenal lobe and ventral nerve chord	540	14527	Excitatory
Drosophila adult (*88*)	Mushroom Body	100	26001	Excitatory
Rat (*86*)	Hippocampus	287	50800	Excitatory
Mouse (*53*)	Neocortex layer 2/3	15	74667	Excitatory
Human (*87*)	Entorhinal cortex (AS)	8794	118492	Excitatory
Human (*87*)	Entorhinal cortex (SS)	550	70501	Inhibitory

Table 3: **Details of species, brain regions and quantification of postsynaptic density area.** The table summarizes the postsynaptic density (PSD) characteristics for various species, including *Drosophila* (larva and adult), rat, mouse, and human. For each species, the specific brain region studied, sample size, and mean area of the PSD in square nanometers (nm^2) are provided. For human data, "AS" denotes asymmetrical synapse, and "SS" symmetrical synapse. References for the data sources are included.

Dataset details used throughout this study						
Dataset	**Synapse density**	**Synapse size**	**Scaling law**	**Radius**	**Synapse location**	**Total**
Drosophila larva (EM)	233	0	233	150	233	233
Drosophila larva mutants (EM)	40	0	40	0	40	40
Drosophila adult (EM)	60 (417†)	0	60	0	60	417
Zebrafish larva (EM)	709	0	709	0	709	709
MICrONS Mouse layer 2/3 (EM)	301	0	301	301	301	301
MICrONS Mouse mm^3 (EM)	1183	1183*	1183	1183	1183	1183
Rat Hippocampus Pyramidal Cell (LM)	0	0	0	47	0	47
Human Neocortical Layer 3 (LM)	0	0	0	99	0	99
Drosophila larva (PSD)	0	540	0	0	0	540
Drosophila Adult (PSD)	0	100	0	0	0	100
Rat (PSD)	0	287	0	0	0	287
Human (PSD)	0	9344	0	0	0	9344

Table 4: **Quantitative summary of number of neurons per dataset used in this study**.
This table provides a detailed overview of the datasets used in the study, specifying the number of neurons used to compute synapse density, synapse size, scaling law based on wiring minimisation, radius, synapse location, and total count of neurons per dataset. ”EM” and ”LM” denote electron microscopy and light microscopy, respectively. ”PSD” denotes postsynaptic density. The entries marked with an asterisk (*) indicate synaptic size data given in number of voxels and not in PSD area nm^2. † Indicates the number of cells used to calculate the postsynaptic reconstruction correlation with synaptic density (**Figure S1**C)

Synaptic quantifications details			
Species	**Synapse density (mean $\pm$ SD)**	**Inter-synaptic distance (mean $\pm$ SD)**	**Spatial location (mean $\pm$ SD)**
Drosophila larva	$\frac{0.96syn}{\mu m} \pm 0.34$	$\frac{1.31syn}{\mu m} \pm 0.49$	0.54 ± 0.06
Drosophila adult	$\frac{0.81syn}{\mu m} \pm 0.22$	$\frac{1.89syn}{\mu m} \pm 0.51$	0.66 ± 0.16
Zebrafish adult	$\frac{0.76syn*}{\mu m} \pm 0.23$	$\frac{1.23syn*}{\mu m} \pm 0.47$	0.31 ± 0.1476
Mouse adult	$\frac{0.99syn}{\mu m} \pm 0.28$	$\frac{1.57syn}{\mu m} \pm 0.45$	0.45 ± 0.07

Table 5: **Quantitative summary of synaptic properties across different cpecies**.
This table provides a quantitative summary of synaptic properties across various species, detailing synaptic density, inter-synaptic distance, and spatial location. The values are presented as mean $\pm$ standard deviation (SD). Spatial location, indicating variability in synapse positioning. The location ranges between $[0-1]$, with value 0 meaning the most proximal, 0.5 is uniformly distributed at random, and 1 the most distal (see Methods). Start sign denotes corrected values (uncorrected zebrafish synaptic density $= \frac{0.31syn}{\mu m} \pm 0.16$; uncorrected zebrafish inter-synaptic distance $= \frac{3.47syn}{\mu m} \pm 2.18$ see Methods)

Acknowledgments

We thank Adrian Wanner and Rainer W Friedrich, Casey Schneider-Mizzel, and Sahil Loomba for sharing the zebrafish, mouse and human datasets, respectively. We thank Tom Bartol for sharing the rat postsynaptic density areas dataset; and Sergio Plaza Alonso, Lidia Alonso-Naclares and Javier Defelipe for sharing the human postsynaptic density areas dataset. We also thank Daniel Han, Philipp Schelegel, Dániel Barabási and Benjanmin Piazza for support in handling various connectomics datasets. The authors thank Marc Corrales for helpful comments in the manuscript. Finally, we thank Ivana Henry for helping design some sketches. We also acknowledge Ingo Fritz, Ricardo Chirif Molina and Feiyu Wang for help collecting postsynaptic density data.

Supported by Wellcome Trust Investigator Award 205038/Z/16/Z to A.C. , and core funding from the MRC LMB. The project was also supported by a Daimler-Benz Grant (A.F.C.).

Author contributions

André Ferreira Castro, Conceptualisation, Resources, Data curation, Investigation, Visualisation, Formal analysis, Methodology, Writing - review and editing; Albert Cardona, Conceptualisation - writing - review and editing.